Homonuclear dual-atom catalysts embedded on N-doped graphene for highly efficient nitrate reduction to ammonia: From theoretical prediction to experimental validation

Tiantian Zhao [a,1], Kai Chen [b,1], Xiaochun Xu [c], Xinyi Li [c], Xiao Zhao [c,*], Qinghai Cai [a], Ke Chu [b,*], Jingxiang Zhao [a,*]

[a] College of Chemistry and Chemical Engineering, and Key Laboratory of Photonic and Electronic Bandgap Materials, Ministry of Education, Harbin Normal University, Harbin 150025, China
[b] School of Materials Science and Engineering, Lanzhou Jiaotong University, Lanzhou 730070, China
[c] State Key Laboratory of Automotive Simulation and Control, School of Materials Science and Engineering, and Key Laboratory of Automobile Materials of MOE, Jilin University, Changchun 130012, China

ARTICLE INFO

ABSTRACT

Electrocatalytic reduction of nitrate (NO_3^-) to ammonia (NRA) is emerging as an attractive strategy to attain valuable NH_3 synthesis and harmful NO_3^- removal, but developing efficient electrocatalysts remains challenging. Herein, taking homonuclear dual metal catalysts (DACs) embedded on N-doped graphene as the example, we proposed a three-step strategy to theoretically evaluate their NRA catalytic performance by means of density functional theory (DFT) computations, which enables us to rapidly identify $Cu_2@N_3-6$ as the most promising NRA catalyst with a low limiting potential (-0.14 V). More importantly, such theoretical prediction was further validated by our proof-of-concept experiment: the NH_3 yield rate of ~18.2 mg h^{-1} cm^{-2} at -0.8 V vs RHE and the Faradaic efficiency of 97.4% were achieved. Our studies may offer a feasible avenue to rapidly and precisely achieve efficient NRA catalysts by using theoretical prediction as a guideline for experimentalists to avoid the traditional "trial and error method".

1. Introduction

Nitrate (NO_3^-) is one of the most common water pollutants from the excessive use of nitrogen−rich fertilizers, the combustion of fossil fuels, and the discharge of wastewater from industrial sources [1–3]. In recent years, the NO_3^- concentration in groundwater has been sharply increased due to the human activities, leading to the great threaten to both environments (such as acid rain and photochemical smog) [4] and human health (such as liver damage, blue baby syndrome, and even cancer) [5, 6]. In this context, the World Health Organization (WHO) has proposed the maximum NO_3^- concentration in drinking water to 50 mg·L^{-1} [7]. At present, some methods have been reported to remove NO_3^- pollutants from water, such as biological, physical, and chemical denitrification methods, but which are expensive and need complex treatment [8–10]. The electrocatalytic reduction holds great potentials as a promising technology for nitrate removal, as it combines the advantages of the

utilization of clean energy and protons directly from water [11–13]. In addition, the other attractive advantage is that such process can efficiently convert NO_3^- into non−toxic nitrogen or valuable ammonia (NH_3), which has been considered as one of the promising alternatives for the traditional Haber−Bosch process to realize the NH_3 synthesis at ambient conditions [14–17]. Thus, the nitrate reduction to ammonia (NRA) has aroused great enthusiasm in recent years, which can effectively realize both sustainable NH_3 production and wastewater purification from the point of turning waste into wealth.

Nonetheless, it is well known that the NRA is a complex reaction process, as it involves the transfer of nine protons and eight electrons along different possible reaction pathways ($NO_3^- + 9 H^+ + 8e^- \rightarrow NH_3 + 3 H_2O$) [18]. Thus, the NRA would remain some challenges from several competitive reactions, including the hydrogen evolution reaction (HER) and the formation of other N−based byproducts (NO, NO_2, N_2, and N_2O), leading to poor NH_3 selectivity [19–21]. Obviously, to achieve the

practical applications of NRA, it is critical to develop stable and low-cost catalysts with high-activity and high-selectivity to boost the NRA process while suppressing the corresponding side reactions [22–24].

As an extension of single atom catalysts (SACs) [25], dual−atom catalysts (DACs) not only inherit all advantages of SACs (such as maximized atom−utilization efficiency), but also exhibit some unique properties [26–28]. For example, DACs can provide two adjacent active sites to synergistically activate reactants and stabilize some key reaction intermediates, which is of great significance to realize the high electrocatalytic performance in multi−step coupled proton−electron transfer process [29–32]. For example, Hao et al. fabricated a catalyst of Ni dual−atom sites, and achieved efficient CO_2 electroreduction (CO_2ER) with a CO partial current density up to ~1 A cm^{-2} and turnover frequency of 77,500 h^{-1} at > 99% Faradaic efficiency [33]. Xie et al. reported copper dimers anchored on graphitic carbon nitride as advanced catalysts for CH_4 partial oxidation [34]. In addition, DACs also hold great promises for the oxygen reduction reaction (ORR) [35], nitrogen reduction reaction (NRR) [36,37], urea synthesis [38,39], and so on [40,41]. Especially, some DACs, such as Cu/Fe [42], Cu/Ni [43], Cu_2 [44], and Cr_2 [45] anchored on N-doped carbon materials were reported to exhibit high catalytic performance for NH_3 production. However, the "trial and error method" is still the traditional strategy in experiments, which undoubtedly wastes a lot of resource and time. On the other hand, although theoretical studies have predicted some promising SACs [46–50] and DACs [44,45] for NRA, the corresponding experimental validation still remains a huge challenge. Thus, it is highly desirable for rapidly and precisely achieving highly efficient NRA catalysts through the theoretical guidance and experimental verification. To the best of our knowledge, there is no prior study on this interesting issue in NRA field.

Herein, we took DACs anchored on nitrogen−doped graphene with different coordination environments (TM_2 @N_x-y, where x represent the coordination number of each TM atom, and y is the total number of N atoms in the substrate) as the example to explore their NRA catalytic performance by means of comprehensive density functional theory (DFT) computations, followed by systematical experimental verification. Based on a three−step screening strategy, the Cu_2@N_3-6 was extracted out from 80 TM_2 @N_x- y candidates as the best NRA catalyst with an ultralow limiting potential (−0.14 V) to achieve its high catalytic activity and the outstanding suppressing effects on the side reactions to ensure its high selectivity toward NH_3 production. More interestingly, the theoretical findings can be validated by our experimental studies: the Cu_2 DAC exhibits superior catalytic performance for NRA with an NH_3 yield of 18.2 mg h^{-1} cm^{-2} and a Farady efficiency of 97.4%.

2. Computational details

All spin−polarized DFT computations were performed using the projector augmented wave (PAW) method [51,52] and the Perdew−Burke−Ernzerhof (PBE) exchange correlation functional [53], as implemented in the Vienna Ab *initio* Simulation Package (VASP) [54, 55]. To describe the possible van der Waals (vdW) interactions, the DFT−D3 method in Grimme's scheme was adopted [56]. A plane−wave cutoff energy of 550 eV was employed, and the convergence threshold was set to 10^{-5} eV and 0.01 eV/Å^{-1} for energy and force, respectively, during the structural relaxation. The N−doped graphene−based substrates were modeled using a (6 × 6) supercell with a vacuum layer of 20 Å to avoid the interaction between periodic images, in which a 3 × 3 × 1 k − point sampling was used in the 2D Brillouin zone. The climbing−image nudged elastic band (CI−NEB) method [57] was used to compute the involved energy barriers, and the charge transfer was computed using the Bader charge analysis [58]. The free energy profile was plotted by computing the free energy change (ΔG) of each elementary step in NRA according to the computational hydrogen electrode (CHE) model Nørskov et al. [59,60]. More details on the CHE

model, the adsorption free energy of nitrate and corrections, as well as the experimental synthesis, characterizations, electrochemical measurements, and the computations on the NH_3 yield and Faradaic efficiency (FE) were summarized in the Electronic Supporting Information (ESI).

3. Results and discussion

3.1. Structures and stabilities of catalyst candidates

Experimentally, DACs anchored on N−doped graphene−based have been successfully synthesized, in which two adjacent metal atoms may be coordinated with nitrogen atoms with different microenvironments, leading to the formation of different metal−nitrogen moieties [61–65]. Here, we chose four extensively−used N−doped graphenes as the substrates to anchor 20 homonuclear transition metal atoms as the DACs, thus generating 80 (4 × 20) TM_2 @N_x-y catalysts in total (TM_2 @$N_x- y$, Fig. 1a). We then investigated the geometric structures of these TM_2 @N_x-y systems. After geometrical optimization, we found that these DACs are in or out of the substrate plane, which is dependent on the sizes of the pores of N−doped graphenes. Specifically, all metal atoms protrude out of the N−doped graphene plane with the monovacancy, resulting in the buckled structures. On the contrary, on other three N−doped graphene substrates with larger pores, most of these DACs can incorporate into the central cavity, forming the in−plane configurations. The distances between two adjacent metal atoms range from 1.79 (for Mo_2/N_3-6') to 6.02 Å (for Cr_2/N_3-6). Such interconnection may endow DACs with synergistic effect to promote their cooperative interaction with the adsorbates in electrocatalysis, facilitating to boost their catalytic activity toward the complex reaction process, which can thus overwhelm their single−atom counterparts [66].

Based on the obtained most configurations, we examined the electrochemical and thermodynamic stabilities of the 80 TM_2 @N_x-y candidates by computing their dissolution potentials (U_{diss}) and the energy difference (ΔE) between the binding energy (E_b) of TM atoms on N−doped graphene and the cohesive energy of TM atoms (E_{coh}) and more computational details were presented in ESI. According to these definitions, $U_{diss} > 0$ and $\Delta E < 0$ of a given DAC suggest its good stability from the electrochemical and thermodynamic perspective. As shown in Fig. 1b, the anchored Au_2 is unstable on the four substrates, whereas the remaining 19 metal dimers are stable electrochemically and thermodynamically according to the above−mentioned criteria. Thus, the catalytic performance of Au dimer for NRA was not further studied.

3.2. Screening procedure of catalyst candidates

NRA is a rather complex reaction process, as a variety of possible reaction intermediates (about 30) and products (about 5) are involved (Fig. S1). Clearly, to fully explore the NRA catalytic performance of the 80 TM_2 @N_x-y candidates, about (80 ×30) = 2400 reaction intermediates should be considered, which will inevitably consume huge computational resource. Thus, an efficient screening strategy is essential and highly desirable. Through a careful analysis for previous studies on the NRA mechanisms [67–73], we noted that the hydrogenation of *NO_x intermediate (including *NO_3, *NO_2, and *NO) and the release of *OH is the most likely limiting steps. On one hand, the NO_x species is a stable molecule with inert N=O or N−O bonds. Its hydrogenation has to activate the strong N=O or N−O bonds, which requires a large energy input, thus leading to a relatively positive free energy change for them. On the other hand, there is a half−filled sp^3 hybrid orbital for *OH intermediate, making it more stable on catalyst surface than that of H_2O with fully filled sp^3 hybrid orbitals. Thus, this step of *OH + H^+ + e^- → H_2O is also a possible potential−determining step (PDS) with an uphill free energy change. Moreover, the chemisorption of NO_3^- is also crucial, which is a prerequisite to initiate the subsequent NRA process. In addition, to guarantee the high selectivity of NRA, the competing HER should be
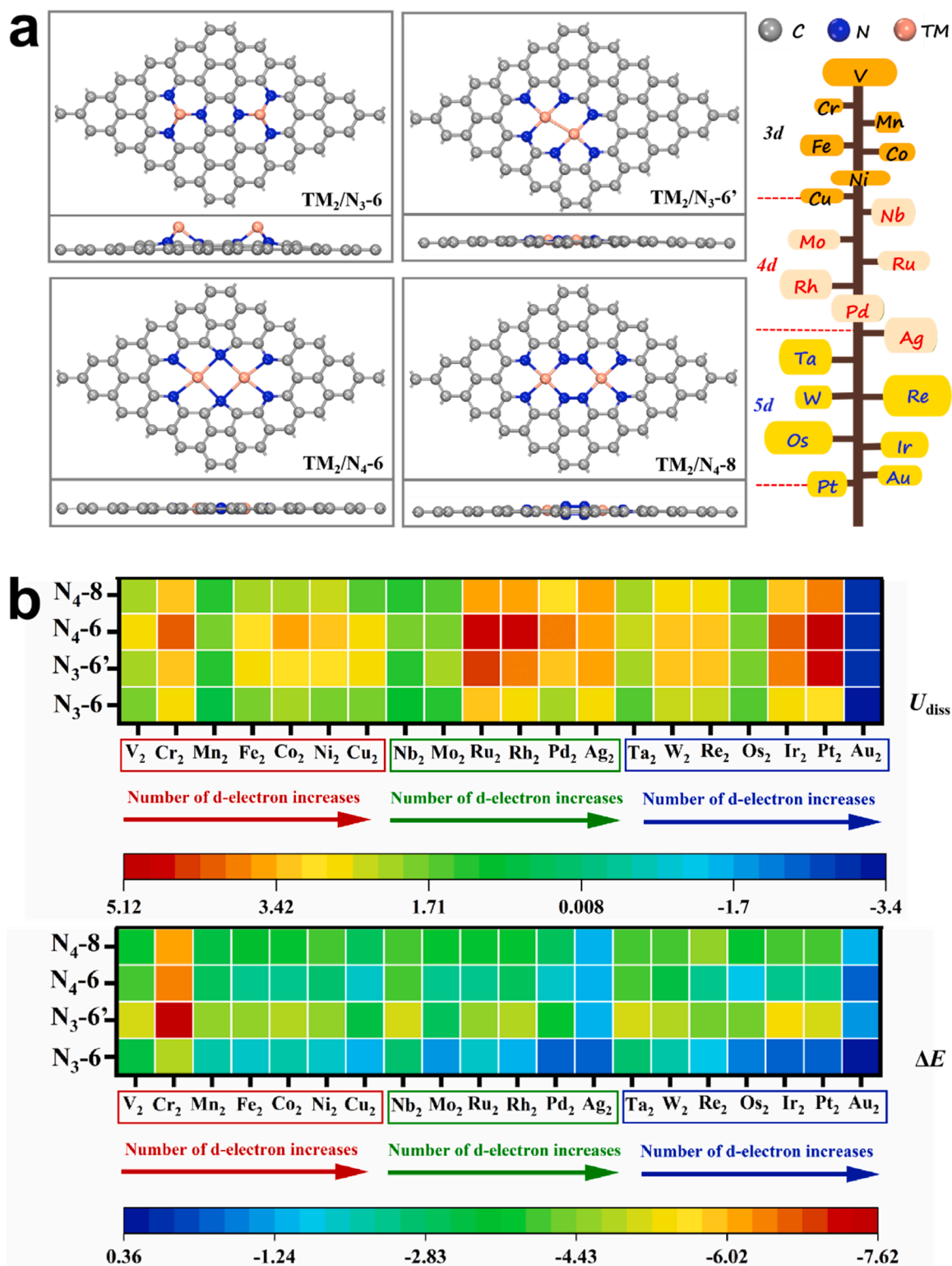
Fig. 1. (a) The considered substrates and metal atoms for constructing the DACs anchored on N−doped graphenes; (b) the computed dissolution potential (U_{diss}) and energy difference (ΔE) between binding energy and cohesive energy for these DACs on different N−doped graphenes.

hindered.

Based on these analysis, a three−step screening strategy was proposed: 1) the free energy change (ΔG) of NO_3^- adsorption should be less than 0 eV to ensure its chemisorption and sufficient activation on the catalyst surface; 2) ΔG for the hydrogenation of $*NO_x$ species and $*OH$ desorption should be smaller than 0.31 eV of the best pure Cu (001)

catalyst [74] to guarantee a higher catalytic activity; 3) the difference of ΔG between NO_3^- and H^+ should be less than 0 eV to ensure a higher selectivity toward NRA by suppressing the competing HER. According to the three−step screening, the whole NRA process on these screened $TM_2/N_x−y$ catalysts will be deeply explored to obtain an exact value of limiting potential (U_L).

First, we examined the NO_3^- adsorption on these DACs, which is a key step to affect or determine the NRA pathway. For transition metal−based DACs, their unoccupied d−orbitals can "pull" the electrons from $*NO_3$ to boost the formation of strong TM−O bonds, whereas their occupied d−orbitals can "push" electrons into anti-bonding orbitals of $*NO_3$ to weaken the N=O bonds, i.e., the so−called "push−pull" hypothesis [75] or the "donation−backdonation" mechanism [76]. To obtain the most stable configuration for NO_3^- adsorption on the catalyst surface, we considered two kinds of adsorption configurations: one or two oxygen atoms of NO_3^- bind with the active sites, forming the η^1-O or η^2-O configuration (Fig. 2a). After structural optimization, we found that the η^2-O-2 configuration on two metal active sites (Fig. 2a) is always the most energetically favorable on all TM_2/N_x-y systems according to the computed $\Delta G*_{NO3}$ values (Table S1), suggesting the excellent synergistic effects between the two active sites on capturing the NO_3^- reactant. Correspondingly, the $\Delta G*_{NO3}$ values for the most stable NO_3^- adsorption on these DACs were presented in Fig. 2b.

Our computations results indicated that, dependent on the kind of DACs and the coordination environment of N−doped graphene, 23 TM_2/N_x-y systems only interact with NO_3^- by physisorption with a positive $\Delta G*_{NO3}$ value, such as Mn_2, Fe_2, Co_2, Ni_2, Cu_2, Rh_2, Pd_2, Ag_2, Ir_2, Pt_2, and Au_2 anchored on N_4-6 substrate (Fig. 2b), suggesting their poor capability for the NO_3^- adsorption and activation, which were thus excluded as the promising NRA catalysts according to the criterion 1. In contrast, NO_3^- reactant can be chemisorbed on the remaining 67 candidates with $\Delta G*_{NO3}$ values between −0.07 and −2.91 eV by the "push−pull" mechanism, which is well consistent with the computed charge density difference (Fig. S2). Especially, TM_2/N_x-y always donates electrons (0.28–1.70 e^-) to the adsorbed $*NO_3$ species, resulting in the N=O bond elongation (1.30–1.47 Å vs 1.25 Å in free NO_3^-) and the sufficient activation of the N=O bond.

To gain an insight into the underlying mechanism of the NO_3^- activation, we analyzed the scaling relationship between the carrying charges (ΔQ) of the active sites and the $\Delta G*_{NO3}$ value. As shown in Fig. 2c, there is a strong scaling relationship between ΔQ and $\Delta G*_{NO3}$ on each type of catalysts with the same coordination conditions, namely, a larger charge transfer induces a stronger NO_3^- adsorption with a more negative $\Delta G*_{NO3}$ value. Furthermore, we computed the crystal orbital Hamilton population (COHP) analysis between metal and O atoms by integrating the band states up to the highest occupied energy level (ICOHP, Fig. 2d), where a more negative value of ICOHP implies a stronger TM−O coupling. The results showed that the computed ICOHPs for NO_3^- adsorption on most of TM_2/N_3-6 are more negative than those on other catalysts. More interestingly, a good linear correlation between ICOHP and $\Delta G*_{NO3}$ can be achieved, well accounting for the adsorption trend NO_3^- on these TM_2/N_x-y catalysts. Intrinsically, the adsorption strength of reaction intermediates is greatly dependent on the electronic characteristics of the active center. To this end, we also computed the d-band centers (ε_d) of the anchored TM atoms. Clearly, there is a similar linear relationship between ε_d and $\Delta G*_{NO3}$ on different kinds of catalysts (Fig. 2e), indicating that the d band center may also be employed to understand the remarkable difference of NO_3^- adsorption on these catalysts.

Noteworthy, according to previous theoretical studies [46–48], $\Delta G*_{NO3}$ can perform as a descriptor to describe the NRA catalytic activity, and too strong and too weak NO_3^- adsorption may require a large energy input in the subsequent some hydrogenation reaction, such as NH_3/H_2O desorption, $*NO_x$ hydrogenation. Thus, according to the Sabatier principle, an optimal NO_3^- binding strength would be beneficial to the whole NRA process. Yet, the detailed quantification of NO_3^- binding strength on various catalysts could be in debate. In particular, since the NRA process involves nine protons and eight electrons transferred and the competition of multiple reaction pathways, some elementary steps are equally important. Thus, it could be not enough to screen out promising NRA catalysts only based on the adsorption strength of some intermediate, such as NO_3^- or HNO_3 species. As such,

we then computed the ΔG values for the hydrogenation of $*OH$, $*NO_3$, $*NO_2$, and $*NO$ intermediates following criterion 2, which were compared with the Cu (100) benchmark due to its low cost and high activity with the ΔG_{max} of 0.31eV. According to our computations, the ΔG values for $*OH$ hydrogenation on the Cu_2/N_3-6, Pd_2/N_3-6, Ag_2/N_3-6, Au_2/N_3-6, Fe_2/N_3-6', Cu_2/N_3-6', Cr_2/N_4-8, Ru_2/N_4-8, Os_2/N_4-8, Co_2/N_4-6, Mo_2/N_4-6, Ru_2/N_4-6, Rh_2/N_4-6, Pd_2/N_4-6, Ir_2/N_4-6, and Au_2/N_4-6 are smaller than 0.31 eV (Fig. 2f), which are thus retained for further exploration. By examining the computed ΔG values for the hydrogenation of $*NO_3$, $*NO_2$, and $*NO$ species (Fig. 2g), however, we found that only the **Cu_2/N_3-6** catalyst satisfied the proposed screening criterion ($\Delta G < 0.31$ eV) with the ΔG values of − 1.02, 0.14, and − 0.02eV, respectively, for the three hydrogenation steps. As expected, too strong NO_3^- adsorption (such as Os_2/N_4-6 with the $\Delta G*_{NO3}$ of −2.91 eV) leads to an ultra-large free energy barrier for $*OH$ desorption (3.87 eV), whereas too weak NO_3^- adsorption (such as Mn_2/N_4-8 with the ΔG_{*NO3} of 0.16 eV) hinders the $*NO$ hydrogenation ($\Delta G = 0.63$ eV for Mn_2/N_4-8). In contrast, only Cu_2/N_3-6 system can comprehensively balance the adsorption strength of all key reaction intermediates in the whole NRA process, which will be favorable to achieve a high NRA catalytic activity as later discussed. In addition, as HER is a main competitive reaction during the NRA, $*H$ may cover the catalyst surface and block the active sites for the NRA. In this context, we further computed the free energy change of $*H$ adsorption ($\Delta G*_H$) on the Cu_2/N_3-6. The results showed that the $\Delta G*_H$ is computed to be 0.69 eV on Cu_2/N_3-6 (Fig. S3), which is much less favorable than $\Delta G*_{NO3}$ of − 0.76 eV, indicating that the $*NO_3$ adsorption significantly suppresses $*H$ on the Cu_2/N_3-6 system. Thus, this Cu_2/N_3-6 catalyst displays high selectivity toward NH_3 production from the NRA process. Overall, only Cu_2/N_3-6 satisfies the proposed three-step screening criterion, which is thus chosen as the promising electrocatalyst for the NRA.

3.3. Electrochemical performance of Cu_2/N_3-6 for NRA

In theory, the intrinsic activity of a given electrocatalyst toward NRA can be estimated by the limiting potential (U_L), which represents the minimum applied potential to ensure all elementary reactions to be exergonic. Then, we explored the detailed reaction pathways of NRA on Cu_2/N_3-6 by considering all possible intermediates with the lowest total free energies to obtain the most energetically favorable free energy diagram, while the free energy changes along other pathways were summarized in Table S2.

The results showed that, due to the synergistic effect, the NO_3^- is preferable to adsorb the two Cu sites by forming two Cu−O bonds with the lengths of 1.93 and 1.99 Å, respectively. Remarkably, this elementary is downhill in the free energy profile by 0.76 eV, which is followed by its hydrogenation to form the $*NO_3H$ by interacting with the H^+/e^- pair. Interestingly, after geometrical optimization, we found that the $*NO_3H$ species is spontaneously dissociated into ($*NO_2 + *OH$), which bind with two Cu active sites. Similar dissociation mechanism was observed for NRA on Ru-doped Co_2P monolayer [71] and Pt/TiO_2 [73]. Notably, in the $*NO_2$ configuration, its N atom is more stable to be adsorbed on the Cu site than O atom by 0.41 eV. Then, a second H^+/e^- pair preferably attack to the adsorbed $*OH$ to form the first water molecule, leaving the $*NO_2$ species with the ΔG of −0.60 eV. The next step is the hydrogenation of $*NO_2$, in which the proton favorably reacts with the O atom to form $*NO_2H$ species. Remarkably, this step is slightly endothermic by 0.14 eV, which is smaller than that of the $*HNO_2$ formation with the ΔG of 0.45 eV. Subsequently, the $*NO_2H$ can be readily hydrogenated to yield the second water molecule and the $*NO$ group, which is highly exothermic by 0.96 eV in the free energy diagram. Next, the remaining $*NO$ species on one of Cu active site with the bond length of 1.77 Å is preferable to be hydrogenated to generate $*HNO$ after overcoming a small potential barrier of 0.02 eV, which is much lower than that of $*NOH$ (1.27 eV). Notably, both N and O atom of $*HNO$ bind with two Cu active sites with the length of 1.90 and 2.03 Å, respectively.

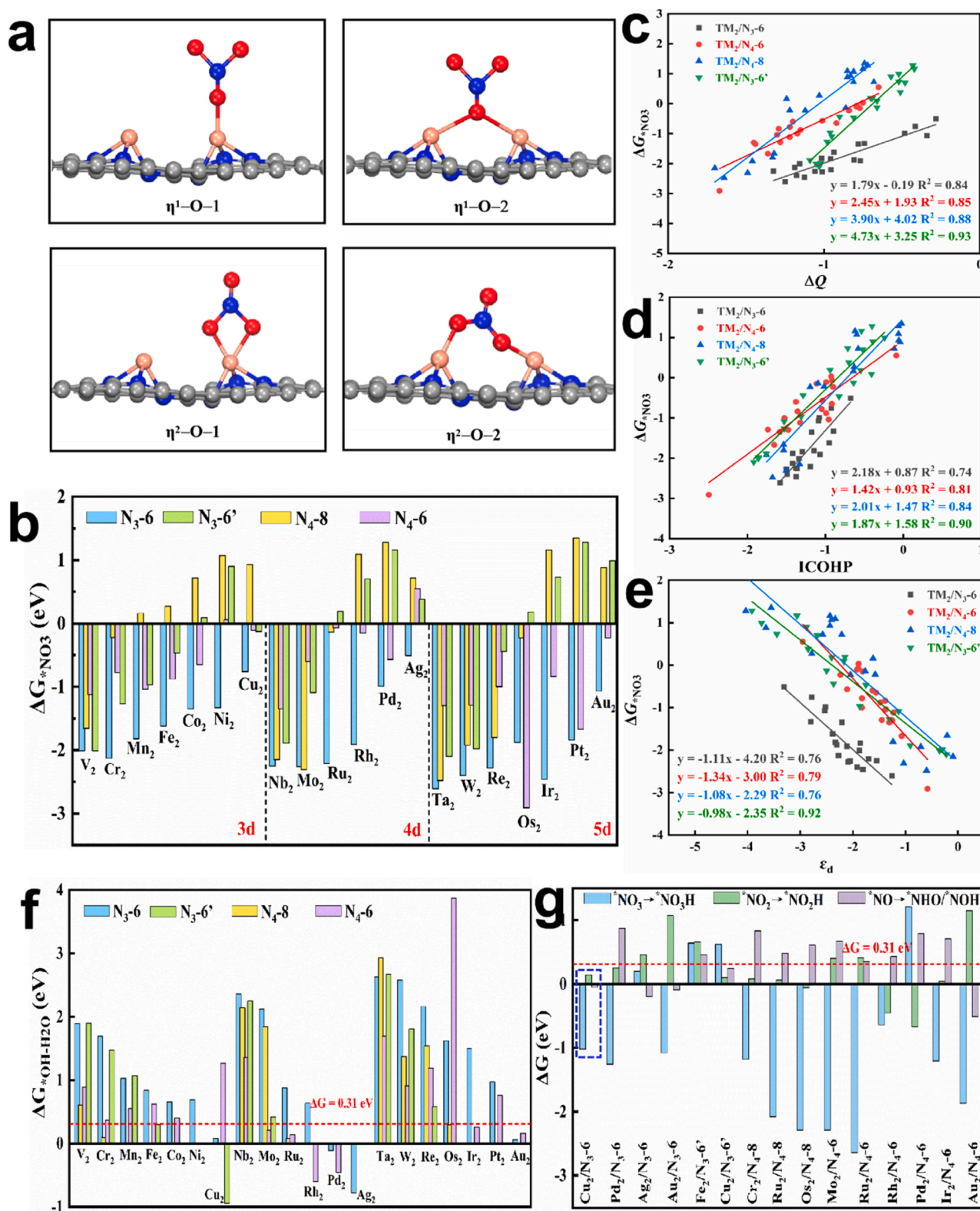**Fig. 2.** (a) The considered initial NO_3^- adsorption configurations by η^1-O and η^2-O patterns; (b) the computed ΔG values for $*NO_3$ adsorption; The variation of free adsorption energies of NO_3^- ($\Delta G*_{NO3}$) with (c) the carrying charge of active sites (ΔQ), (d) the integrated-crystal orbital Hamilton population (ICOHP) of the formed TM-O bonds, and (e) the d-band center (ε_d) of active sites. The computed ΔG values for the hydrogenation of (f) $*OH$ and (g) $*NO_3$, $*NO_2$, and $*NO$ species on various TM_2/N_x-y catalysts.

Next, the protons consecutively attacks the N atom of *HNO to generate NH_3 product via the *H_2NO intermediate. Especially, the processes of *HNO →*H_2NO → *O + NH_3 are exothermic by 0.07 and 2.19 eV, respectively. Finally, the bound *O on Cu site with the length of 1.72 Åcan be converted into the third water molecule through two hydrogenation steps with the ΔG values of −1.64 and 0.08 eV, respectively.

In Fig. 3, we summarized the obtained free energy profile and the corresponding adsorption configurations for various intermediates of NRA on Cu_2/N_3−6, which prefers to proceed thermodynamically along the following pathway: NO_3^- → *NO_3 → *NO_2 + *OH → *NO_2 → *NO_2H → *NO → *HNO →*H_2NO → *O + NH_3 → *OH → H_2O. Among all elementary steps, the hydrogenation of *NO_2 to *NO_2H was identified as the PDS due to its maximum ΔG value of 0.14 eV, corresponding to a rather low U_L of − 0.14 V. For comparison, on the Cu SAC counterpart, the hydrogenation of *NO_3 is the PDS with a much higher limiting potential of − 1.10 V due to its poor activity toward NO_3^- activation (Fig. S4). The higher NRA catalytic activity of Cu_2/N_3−6 catalyst than its SAC counterpart mainly originates from the synergetic effect between two Cu active sites. As shown in Fig. 3, the H approach induces the dissociation of *NO_3 species into (*NO_2 + *OH), which are adsorbed on the two Cu sites separately, reflecting the obvious synergistic effects of DAC on the activation of the adsorbed *NO_3 species. Due to the only single active site, however, the *NO_3 hydrogenation on Cu SAC is rather difficult (Fig. S4), making it become the PDS of NRA on Cu SAC and thus requiring a rather high energy input (1.10 eV). In this sense, the synergetic effect within Cu_2/N_3−6 system plays an important role on boosting the NRA catalytic activity by sufficiently activating NO_3^- reactant. Moreover, the kinetics of the proton-transfer in PDS using the $H_5O_2^+$ as the solvated proton donor was also examined. The results showed that the computed activation barrier of PDS at the 0.00 V is as low as 0.70 eV on the Cu_2/N_3−6 catalyst (Fig. S5), which can be easily surmountable at room temperature or diminished with more negative applied voltages. In addition, using an implicit solvation model implemented in VASPsol [77], we found that the solvation effect almost does not affect the catalytic activity of Cu_2/N_3−6 with a negligible U_L change of 0.03 V (from −0.14 to −0.11 V, Fig. S6). To summarize, our proposed Cu_2/N_3−6 exhibits a rather high NRA catalytic activity due to its ultra−low limiting potential of − 0.14 V, which is twice less than that on the Cu(001) surface (−0.31 V) [74] and most of reported

electrocatalysts (Table S3). Notably, in addition to TM_2/N_3−6 candidates in Fig. 1a, other two possible TM_2/N_3−6 models were also considered due to the difficulty in distinguishing the exact structure through experiments [78,79]. Limited by space in Figs. 1 and 2, the corresponding results were summarized in Fig. S7. Based on the aforementioned three−step screening strategy, we found that all these candidates exhibit weaker NRA catalytic activity than Cu_2/N_3−6 catalyst due to their required higher energy input (0.50 ∼ 3.27 eV) for NO_3^- activation, *NO_x hydrogenation, or *OH desorption. Thus, only Cu_2/N_3−6 was focused in the following discussion.

During the NRA process, several other N-based byproducts may be generated, including NO, NO_2, N_2O, and N_2. To further examine the selectivity of NRA toward NH_3, we explored the possibility of NO_2, NO, N_2O, and N_2 formation on Cu_2/N_3−6 catalyst. As shown in Fig. 3, the free energy barriers for the release of NO_2 and NO is as high as 1.84 and 1.39 eV, respectively, which is much larger than those of their hydrogenation to *NO_2H (0.14 eV) and *HNO (0.02 eV) on Cu_2/N_3−6, respectively, suggesting that the formation of the two byproducts is almost impossible at ambient conditions. Moreover, as for the formation of N_2O and N_2, the coupling of two *NO species to (NO)$_2$ intermediate is a crucial step. Remarkably, the kinetic barrier for this process reaches up to 1.91 eV (Fig. S8) due to the large distance between two Cu active sites (∼5.70 Å),thus hampering the *NO coupling, much less the generation of N_2O and N_2. Thus, the high-selectivity NRA toward NH_3 product can be achieved on the Cu_2/N_3 − 6 catalyst. In addition, under the working conditions of NRA, the metal−based active sites might be oxidized by −OH or –O in aqueous solution, inducing the decreased reactive sites and thus hampering the NRA process. To address this question, the surface Pourbaix diagram of Cu_2/N_3 − 6 catalyst was constructed to identify the possible surface configurations under different equilibrium potentials and pH values. Our results indicated that when the electrode potential is 0 V vs standard hydrogen electrode, the Cu_2/N_3 − 6 surface is fully covered by *O and *OH species, independent of the pH value. However, once an electrode potential is applied, the covered *O and *OH will be hydrogenated. Interestingly, the required minimum potentials (U_R) to remove *O/*OH species on Cu_2/N_3 − 6 surface at pH = 0 is about 0.02 V (Fig. S9), which is less negative than the corresponding U_L for NH_3 synthesis from NRA (−0.14 V), excluding the possibility of its surface oxidation under working conditions and
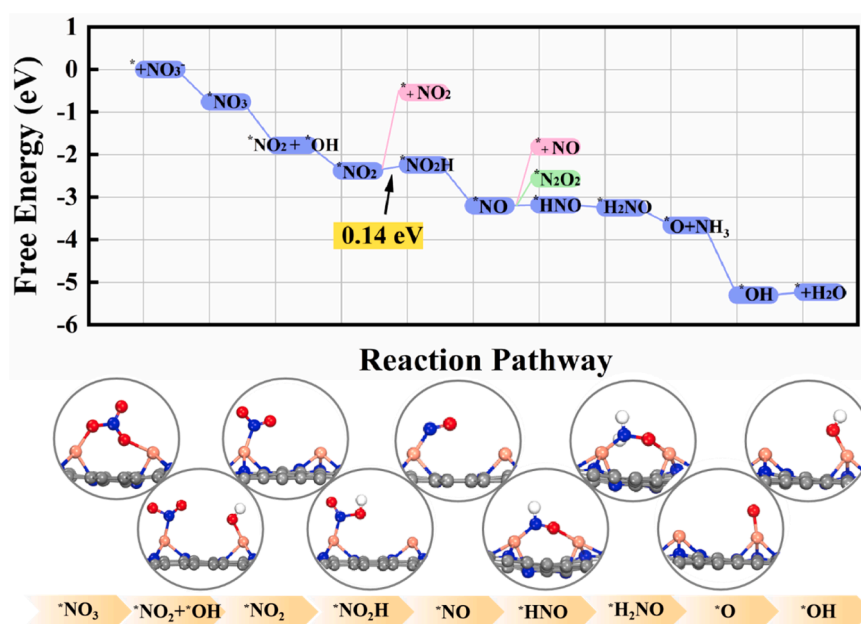

Fig. 3. The computed free energy diagram of NRA on the Cu_2/N_3−6 catalysts and the involved intermediates. The pathways to the release of NO_2, NO, and the formation of *N_2O_2 were also plotted for comparison.

guaranteeing the high activity of $Cu_2/N_3 - 6$ toward NRA process.

3.4. Proof-of-concept experiment

Encouraged by the above theoretical results, the proof-of-concept experiments were then conducted. The diatomic Cu catalyst containing predominantly Cu_2/N_3-6 moieties (defined as Cu_2/N_3-6, Cu: 0.62 wt%) was synthesized using a facile pyrolysis method. Representative TEM image of Cu_2/N_3-6 (Fig. 4a) presents the graphene-like wrinkled nanosheet morphology. The XRD pattern of Cu_2/N_3-6 (Fig. S10) shows two broad reflections at $2\theta = 24°$ and $44°$ ascribed to the (002) and (100) planes of carbon [80]. No XRD peaks related to Cu or Cu_xO species are observed, suggesting that the Cu species are present in an ultrasmall and highly dispersed state on the carbon matrix of Cu_2/N_3 –6. As revealed in Fig. 4b, the AC-HAADF-STEM image displays a multitude of atomically dispersed bright dots, which are assigned to isolated Cu atoms anchored on the carbon matrix. Notably, such automatically isolated Cu atoms are predominantly existed in the form of Cu pairs, as marked by yellow circles [81]. This observation can be further attested by the atomic intensity line scanning profile (Fig. 4c) and topographic atom images (Fig. 4d) [82]. Further, we conducted a statistical analysis of 100 isolated Cu atoms (Fig. S11) and found that the majority of Cu–Cu diatomic distances lie in the range from 5.5 to 6.0 Å, in general accordance with that calculated from an optimized DFT

model (5.7 Å, Fig. 4g, inset). It is worth noting that the presence of surface wrinkles may lead to non-parallel alignment of the coaxial line of Cu pairs along the nanosheet plane [83]. As such, some Cu–Cu diatomic distances are smaller than 5.5 Å. Element mapping images (Fig. 4e) unveil the uniformly distributed C, N, Cu elements in Cu_2/N_3-6.

We then performed XAS measurements to investigate the chemical states and coordination environment of Cu_2/N_3-6. The Cu K-edge XANES spectra (Fig. S12) reveal that the absorption edge of Cu_2/N_3-6 is located between that of Cu_2O and CuO references, suggesting the positively charged $Cu^{\delta+}$ ($1 < \delta < 2$) in Cu_2/N_3-6. In the Cu K-edge EXAFS spectrum of Cu_2/N_3-6 (Fig. 4f), only the dominant peak at ~1.45 Å assigned to the Cu–N coordination is observed, while the Cu–Cu coordination is absent, verifying that Cu atoms in $Cu_2/N_3 - 6$ are atomically dispersed and stabilized by N coordination [84]. The atomic isolation of Cu atoms can be further confirmed by the corresponding wavelet transform (WT) contour maps (Fig. 4h), delivering the dominant Cu-N intensity maximum with no presence of Cu–Cu intensity maximum. The best EXAFS quantitative fitting result (Fig. 4g, Table S4) confirms the $Cu_2/N_3 - 6$ configuration which comprises two adjacent Cu_1/N_3 units where each isolated Cu atom is coordinated with three surrounding N atoms.

The NRA performance of Cu_2/N_3-6 was investigated in a typical H-type cell containing 0.5 M Na_2SO_4 + 0.1 M $NaNO_3$ as electrolyte [24]. The LSV curves (Fig. 5a) reveal that Cu_2/N_3-6 exhibits a
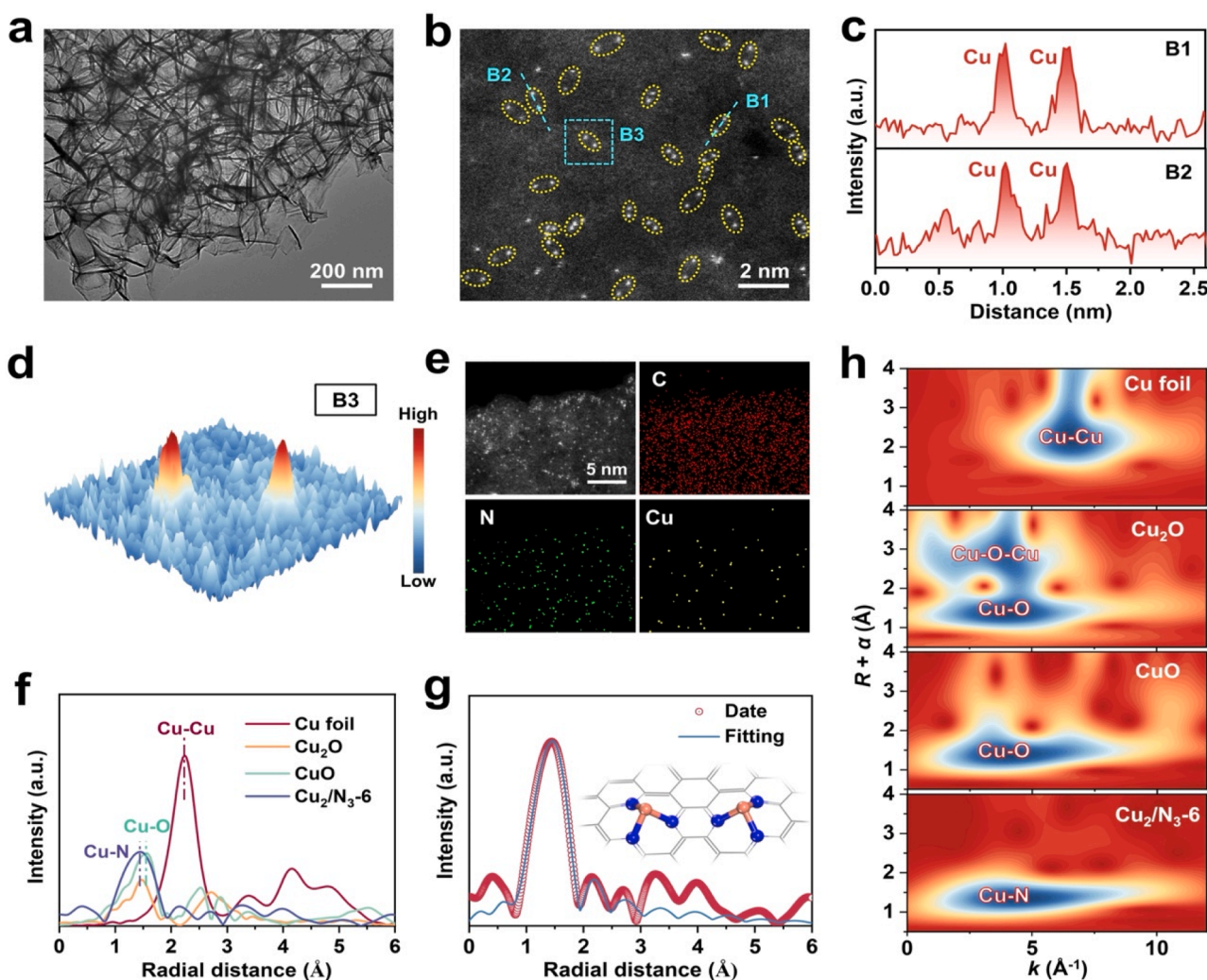

Fig. 4. Characterizations of Cu_2/N_3-6 catalyst: (a) TEM image. (b) AC−HAADF−STEM image and corresponding (c) intensity line scanning profile and (d) 3D topographic atom image. (e) STEM element mapping. (f) Cu K−edge EXAFS spectra and (h) WT contour maps of Cu_2/N_3-6 and reference samples of Cu foil, Cu_2O and CuO. (g) EXAFS fitting curve (inset: fitting model).
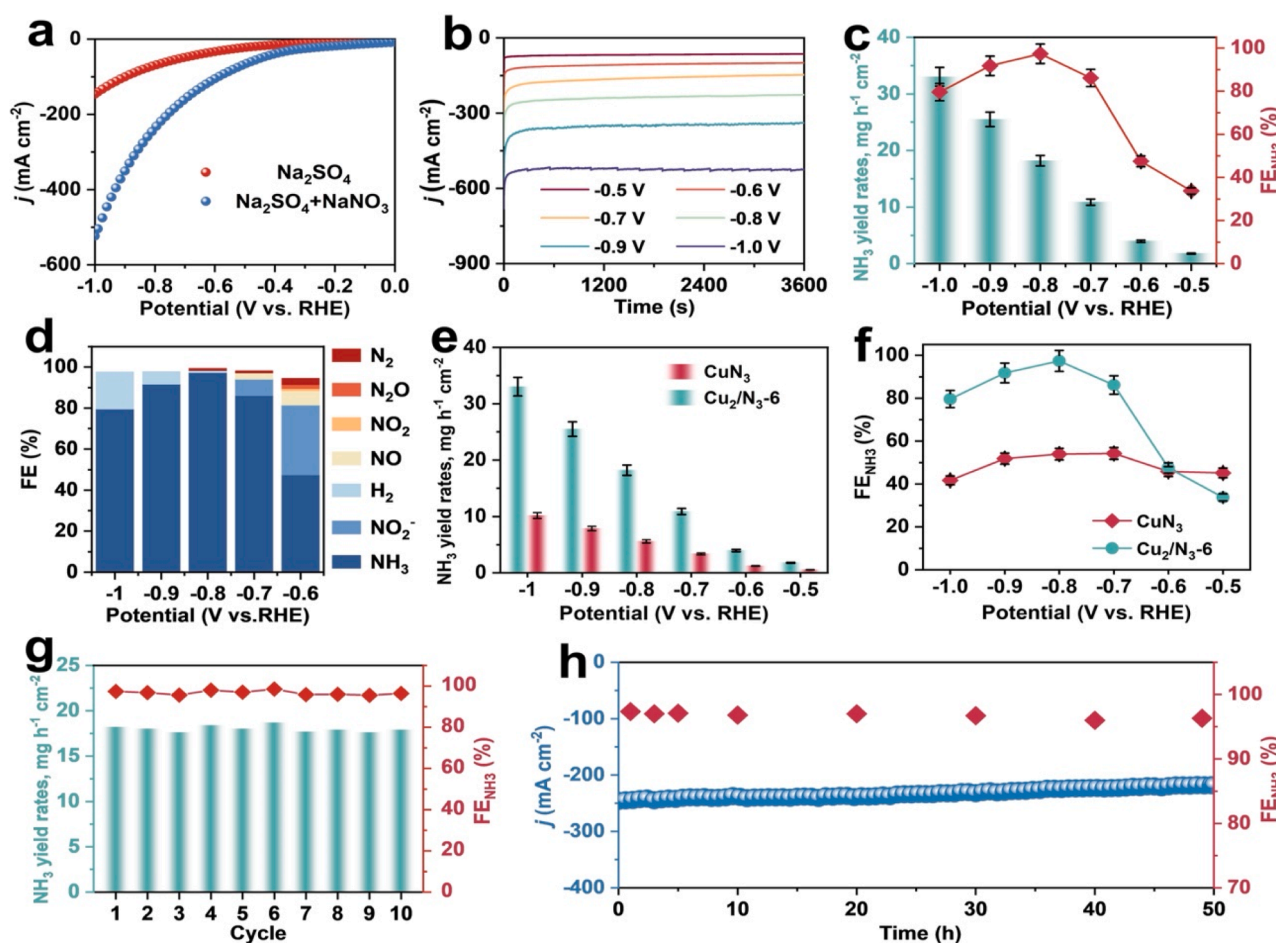
Fig. 5. LSV curves of Cu$_2$/N$_3$−6 in 0.5 M Na$_2$SO$_4$ with and without 0.1 M NO$_3^-$. (b) Potential dependent chronoamperometry curves of Cu$_2$/N$_3$−6 after 1 h of NRA electrolysis. (c) NH$_3$ yield rates and FE$_{NH3}$ of Cu$_2$/N$_3$−6 at various potentials. (d) FEs of various products. Comparison of the (e) NH$_3$ yield rates and (f) FE$_{NH3}$ of Cu$_2$/N$_3$−6 and CuN$_3$ at various potentials. (g) Cycling and (h) long-term chronoamperometry tests at − 0.8 V.

significantly enhanced current density (*j*) in NO$_3^-$−containing electrolyte relative to NO$_3^-$−free electrolyte, indicating the high NRA activity of Cu$_2$/N$_3$−6. Then the NRA performance of Cu$_2$/N$_3$−6 was quantified by the combined chronoamperometry (Fig. 5b) and UV−vis spectrophotometry (Fig. S13) experiments at various applied potentials [14]. After diluting the post−electrolysis electrolytes, the gas and liquid products were quantified by gas chromatography (GC) and colorimetric approaches (Fig. S14−S15), respectively. As displayed in Fig. 5c, the FE$_{NH3}$ of Cu$_2$/N$_3$−6 exhibits a volcanic shape at various potentials, achieving a maximal value of 97.4% at − 0.8 V with a corresponding NH$_3$ yield rate of 18.2 mg h^{-1} cm^{-2}, surpassing that of most reported NRA catalysts as summarized in Table S5. The control chronoamperometry experiments (Fig. S16) and ^{1}H NMR measurements (Fig. S17) validate that the detected NH$_3$ is generated via NRA process on Cu$_2$/N$_3$−6 [85].

We also monitored the possible byproducts during the NAR process, including NO$_2^-$, H$_2$, NO, NO$_2$, N$_2$O, and N$_2$, with their corresponding FEs displayed in Fig. 5d. It is seen that NO$_2^-$ is the main byproduct at potentials lower than − 0.8 V. This can be mainly attributed to the relatively difficult conversion of *NO$_2$ to *NO$_2$H on Cu$_2$/N$_3$−6, which is the PDS of the NRA with an activation barrier of 0.7 eV, leading to the accumulation of NO$_2^-$ in the electrolyte during electrolysis. With further increasing potentials beyond − 0.8 V, H$_2$ becomes the major byproduct due to the enhanced HER [85]. Meanwhile, at all applied potentials, the amounts of other N-containing byproducts are negligible, indicating the high selectivity of Cu$_2$/N$_3$−6 for the direct conversion of NO$_3^-$ to NH$_3$. We also synthesized Cu sing atom catalyst with isolated Cu−N$_3$ (Cu−N$_3$, Fig. S18) and evaluated its NRA performance. It is observed that both

NH$_3$ yield rates (Fig. 5e) and FE$_{NH3}$ (Fig. 5f) of CuN$_3$ are significantly lower than those of Cu$_2$/N$_3$−6. Besides, the NRA performance normalized by electrochemical surface area (ECSA, Fig. S19) delivers the same trend with Fig. 5e and f (Fig. S20), suggesting the remarkable synergistic effect of Cu diatomic sites in greatly promoting the NRA activity and selectivity. The much higher NH$_3$-TOF of Cu$_2$/N$_3$–6 compared to CuN$_3$ also demonstrate its superior inherent catalytic activity for NH$_3$ synthesis (Fig. S21). Regarding the electrocatalytic stability of Cu$_2$/N$_3$−6, through ten successive electrolysis cycles (Fig. 5g), the NH$_3$ yield rates and FE$_{NH3}$ remain nearly consistent, verifying a good cycling stability of Cu$_2$/N$_3$−6. In addition, over 50 h continuous electrolysis at − 0.8 V (Fig. 5h), Cu$_2$/N$_3$−6 presents stable current density and well-maintained FE$_{NH3}$, confirming its excellent long-term durability. The morphology (Fig. S22a) and diatomic coordination structure (Fig. S22b–d) of Cu$_2$/N$_3$−6 are well retained after long–term chronoamperometry test, suggesting the robust structural durability of Cu$_2$/N$_3$−6. These experimental results demonstrate the effectiveness of our theoretical strategy for precisely screening promising diatomic catalysts for the NRA.

4. Conclusions

In summary, we first investigated the feasibility of a large number of homonuclear DACs anchored on N-doped graphenes as the NRA catalysts by performing DFT computations. The results revealed that the synergistic effects of two active sites contribute to the sufficient activation of NO$_3^-$ reactant, which can be highly related with the intrinsic d−band centers of active sites. Furthermore, through a three-step

screening strategy, we theoretically predicted that Cu_2/N_3-6 catalyst exhibits superior NRA catalytic performance with high-efficiency and high-selectivity. Finally, the systematical experiments validate our theoretical prediction: a NH_3 yield rate and a FE are 18.2 mg h^{-1} cm^{-2} and a FE of 97.4% at -0.8 V vs. RHE were achieved.

CRediT authorship contribution statement

Tiantian Zhao: Conceptualization, Investigation, Formal analysis, Writing – original draft. **Kai Chen**: Methodology, Validation, Investigation, Writing – original draft. **Xiaochun Xu**: Synthesis of catalysts. **Xinyi Li**: Data curation. **Xiao Zhao**: Resources, Visualization. **Qinghai Cai**: Methodology. **Ke Cu**: Project administration, Writing – review & editing. **Jingxiang Zhao**: Conceptualization, Writing – review & editing, Supervision, Funding acquisition.

Declaration of Competing Interest

The authors declare no competing financial interest.

Data Availability

Data will be made available on request.

Acknowledgement

Appendix A. Supporting information

Supplementary data associated with this article can be found in the online version at doi:10.1016/j.apcatb.2023.123156.

References

[1] M. Duca, M.T.M. Koper, Powering denitrification: the perspectives of electrocatalytic nitrate reduction, Energy Environ. Sci. 5 (2012) 9726–9742.

[2] A. Bhatnagar, M. Sillanpää, A review of emerging adsorbents for nitrate removal from water, Chem. Eng. J. 168 (2011) 493–504.

[3] N. Gruber, J.N. Galloway, An earth-system perspective of the global nitrogen cycle, Nature 451 (2008) 293–296.

[4] K. Wick, C. Heumesser, E. Schmid, Groundwater nitrate contamination: factors and indicators, J. Environ. Manag. 111 (2012) 178–186.

[5] N.S. Bryan, D.D. Alexander, J.R. Coughlin, A.L. Milkowski, P. Boffetta, Ingested nitrate and nitrite and stomach cancer risk: an updated review, Food Chem. Toxicol. 50 (2012) 3646–3665.

[6] R. Picetti, M. Deeney, S. Pastorino, M.R. Miller, A. Shah, D.A. Leon, A.D. Dangour, R. Green, Nitrate and nitrite contamination in drinking water and cancer risk: a systematic review with meta-analysis, Environ. Res. 210 (2022), 112988.

[7] M. Parvizishad, A. Dalvand, A.H. Mahvi, F. Goodarzi, A review of adverse effects and benefits of nitrate and nitrite in drinking water and food on human health, Health Scope 6 (2017), e14164.

[8] W. Yang, J. Wang, R. Chen, L. Xiao, S. Shen, J. Li, F. Dong, Reaction mechanism and selectivity regulation of photocatalytic nitrate reduction for wastewater purification: progress and challenges, J. Mater. Chem. A. 10 (2022) 17357–17376.

[9] Y. Wang, C. Wang, M. Li, Y. Yu, B. Zhang, Nitrate electroreduction: mechanism insight, in situ characterization, performance evaluation, and challenges, Chem. Soc. Rev. 50 (2021) 6720–6733.

[10] X. Zhang, Y. Wang, C. Liu, Y. Yu, S. Lu, B. Zhang, Recent advances in non-noble metal electrocatalysts for nitrate reduction, Chem. Eng. J. 403 (2021), 126269.

[11] H. Xu, Y. Ma, J. Chen, W.-x Zhang, J. Yang, Electrocatalytic reduction of nitrate – a step towards a sustainable nitrogen cycle, Chem. Soc. Rev. 51 (2022) 2710–2758.

[12] G. Zhang, X. Li, K. Chen, Y. Guo, D. Ma, K. Chu, Tandem electrocatalytic nitrate reduction to ammonia on MBenes, Angew. Chem. Int. Ed. 62 (2023), e202300054.

[13] X. Yang, S. Mukherjee, T. O'Carroll, Y. Hou, M.R. Singh, J.A. Gauthier, G. Wu, Achievements, challenges, and perspectives on nitrogen electrochemistry for carbon-neutral energy technologies, Angew. Chem. Int. Ed. 62 (2023), e202215938.

[14] N. Zhang, G. Zhang, P. Shen, H. Zhang, D. Ma, K. Chu, Lewis acid Fe-V pairs promote nitrate electroreduction to ammonia, Adv. Funct. Mater. 33 (2023) 2211537.

[15] X. Yang, R. Wang, S. Wang, C. Song, S. Lu, L. Fang, F. Yin, H. Liu, Sequential active-site switches in integrated Cu/Fe-TiO$_2$ for efficient electroreduction from nitrate into ammonia, Appl. Catal. B Environ. 325 (2023), 122360.

[16] K. Wang, R. Mao, R. Liu, J. Zhang, X. Zhao, Sulfur-dopant-promoted electrocatalytic reduction of nitrate by a self-supported iron cathode: Selectivity, stability, and underlying mechanism, Appl. Catal. B Environ. 319 (2022), 121862.

[17] P.H. van Langevelde, I. Katsounaros, M.T.M. Koper, Electrocatalytic nitrate reduction for sustainable ammonia production, Joule 5 (2021) 290–294.

[18] S. Garcia-Segura, M. Lanzarini-Lopes, K. Hristovski, P. Westerhoff, Electrocatalytic reduction of nitrate: fundamentals to full-scale water treatment applications, Appl. Catal. B Environ. 236 (2018) 546–568.

[19] H. Shin, S. Jung, S. Bae, W. Lee, H. Kim, Nitrite reduction mechanism on a Pd surface, Environ. Sci. Technol. 48 (2014) 12768–12774.

[20] J. Gao, B. Jiang, C. Ni, Y. Qi, X. Bi, Enhanced reduction of nitrate by noble metal-free electrocatalysis on P doped three-dimensional Co$_3$O$_4$ cathode: Mechanism exploration from both experimental and DFT studies, Chem. Eng. J. 382 (2020), 123034.

[21] R. Zhang, D. Shuai, K.A. Guy, J.R. Shapley, T.J. Strathmann, C.J. Werth, Elucidation of nitrate reduction mechanisms on a Pd-In bimetallic catalyst using isotope labeled nitrogen species, ChemCatChem 5 (2013) 313–321.

[22] J.-X. Liu, D. Richards, N. Singh, B.R. Goldsmith, Activity and selectivity trends in electrocatalytic nitrate reduction on transition metals, ACS Catal. 9 (2019) 7052–7064.

[23] I. Katsounaros, On the assessment of electrocatalysts for nitrate reduction, Curr. Opin. Electro 28 (2021), 100721.

[24] X. Li, P. Shen, X. Li, D. Ma, K. Chu, Sub-nm RuO$_x$ clusters on Pd metallene for synergistically enhanced nitrate electroreduction to ammonia, ACS Nano 17 (2023) 1081–1090.

[25] B. Qiao, A. Wang, X. Yang, L.F. Allard, Z. Jiang, Y. Cui, J. Liu, J. Li, T. Zhang, Single-atom catalysis of CO oxidation using Pt$_1$/FeO$_x$, Nat. Chem. 3 (2011) 634–641.

[26] J. Wang, C. Liu, S. Li, Y. Li, Q. Zhang, Q. Peng, J.S. Tse, Z. Wu, Advanced electrocatalysts with dual-metal doped carbon materials: Achievements and challenges, Chem. Eng. J. 428 (2022), 132558.

[27] Y. Ying, X. Luo, J. Qiao, H. Huang, More is Different:" synergistic effect and structural engineering in double-atom catalysts, Adv. Funct. Mater. 31 (2021) 2007423.

[28] S. Zhang, Y. Wu, Y.-X. Zhang, Z. Niu, Dual-atom catalysts: controllable synthesis and electrocatalytic applications, Sci. Chi. Chem. 64 (2021) 1908–1922.

[29] W.-H. Li, J. Yang, D. Wang, Long-Range interactions in diatomic catalysts boosting electrocatalysis, Angew. Chem. Int. Ed. 61 (2022), e202213318.

[30] Q. An, J. Jiang, W. Cheng, H. Su, Y. Jiang, Q. Liu, Recent advances in dual-atom site catalysts for efficient oxygen and carbon dioxide electrocatalysis, Small Methods 6 (2022) 2200408.

[31] H. Liu, H. Rong, J. Zhang, Synergetic dual-atom catalysts: the next boom of atomic catalysts, ChemSusChem 15 (2022), e202200498.

[32] Y.-X. Zhang, S. Zhang, H. Huang, X. Liu, B. Li, Y. Lee, X. Wang, Y. Bai, M. Sun, Y. Wu, S. Gong, X. Liu, Z. Zhuang, T. Tan, Z. Niu, General synthesis of a diatomic catalyst library via a macrocyclic precursor-mediated approach, J. Am. Chem. Soc. 145 (2023) 4819–4827.

[33] Q. Hao, H.-x Zhong, J.-z Wang, K.-h Liu, J.-m Yan, Z.-h Ren, N. Zhou, X. Zhao, H. Zhang, D.-x Liu, X. Liu, L.-w Chen, J. Luo, X.-b Zhang, Nickel dual-atom sites for electrochemical carbon dioxide reduction, Nat. Synth. 1 (2022) 719–728.

[34] P. Xie, P. Ding, Z. Yao, T. Pu, P. Zhang, Z. Huang, C. Wang, J. Zhang, N. Zecher-Freeman, H. Zong, D. Yuan, S. Deng, R. Shahbazian-Yassar, C. Wang, Oxo dicopper anchored on carbon nitride for selective oxidation of methane, Nat. Commun. 13 (2022) 1375.

[35] J. Wang, W. Liu, G. Luo, Z. Li, C. Zhao, H. Zhang, M. Zhu, Q. Xu, X. Wang, C. Zhao, Y. Qu, Z. Yang, T. Yao, Y. Li, Y. Lin, Y. Wu, Y. Li, Synergistic effect of well-defined dual sites boosting the oxygen reduction reaction, Energy Environ. Sci. 11 (2018) 3375–3379.

[36] X. Lv, W. Wei, B. Huang, Y. Dai, T. Frauenheim, High-throughput screening of synergistic transition metal dual-atom catalysts for efficient nitrogen fixation, Nano Lett. 21 (2021) 1871–1878.

[37] H. Li, Z. Zhao, Q. Cai, L. Yin, J. Zhao, Nitrogen electroreduction performance of transition metal dimers embedded into N-doped graphene: a theoretical prediction, J. Mater. Chem. A. 8 (2020) 4533–4543.

[38] X. Zhang, X. Zhu, S. Bo, C. Chen, M. Qiu, X. Wei, N. He, C. Xie, W. Chen, J. Zheng, P. Chen, S.P. Jiang, Y. Li, Q. Liu, S. Wang, Identifying and tailoring C–N coupling site for efficient urea synthesis over diatomic Fe–Ni catalyst, Nat. Commun. 13 (2022) 5337.

[39] L. Pan, J. Wang, F. Lu, Q. Liu, Y. Gao, Y. Wang, J. Jiang, C. Sun, J. Wang, X. Wang, Single-atom or dual-atom in TiO$_2$ nanosheet: Which is the better choice for electrocatalytic urea synthesis? Angew. Chem. Int. Ed. 62 (2023) e202216835.

[40] K. Liu, J. Li, Y. Liu, M. Wang, H. Cui, Dual metal atom catalysts: advantages in electrocatalytic reactions, J. Energy Chem. 79 (2023) 515–534.

[41] R. Li, D. Wang, Superiority of dual-atom catalysts in electrocatalysis: One step further than single-atom catalysts, Adv. Energy Mater. 12 (2022) 2103564.

[42] S. Zhang, J. Wu, M. Zheng, X. Jin, Z. Shen, Z. Li, Y. Wang, Q. Wang, X. Wang, H. Wei, Fe/Cu diatomic catalysts for electrochemical nitrate reduction to ammonia, Nat. Commun. 14 (2023) 3634.

[43] Y. Wang, H. Yin, F. Dong, X. Zhao, Y. Qu, L. Wang, Y. Peng, D. Wang, W. Fang, J. Li, N-coordinated Cu–Ni dual-single-atom catalyst for highly selective electrocatalytic reduction of nitrate to ammonia, Small (2023), 2207695.

[44] P. Lv, D. Wu, B. He, X. Li, R. Zhu, G. Tang, Z. Lu, D. Ma, Y. Jia, An efficient screening strategy towards multifunctional catalysts for the simultaneous

electroreduction of NO_3^-, NO_2^- and NO to NH_3, J. Mater. Chem. A. 10 (2022) 9707–9716.

[45] F. Rehman, S. Kwon, C.B. Musgrave III, M. Tamtaji, W.A. Goddard III, Z. Luo, High-throughput screening to predict highly active dual-atom catalysts for electrocatalytic reduction of nitrate to ammonia, Nano Energy 103 (2022), 107866.

[46] H. Niu, Z. Zhang, X. Wang, X. Wan, C. Shao, Y. Guo, Theoretical insights into the mechanism of selective nitrate-to-ammonia electroreduction on single-atom catalysts, Adv. Funct. Mater. 31 (2021) 2008533.

[47] S. Wang, H. Gao, L. Li, K. San Hui, D.A. Dinh, S. Wu, S. Kumar, F. Chen, Z. Shao, K. N. Hui, High-throughput identification of highly active and selective single-atom catalysts for electrochemical ammonia synthesis through nitrate reduction, Nano Energy 100 (2022), 107517.

[48] L. Yang, S. Feng, W. Zhu, Tuning nitrate electroreduction activity via an equilibrium adsorption strategy: a computational study, J. Phys. Chem. Lett. 13 (2022) 1726–1733.

[49] Y. Wang, M. Shao, Theoretical screening of transition metal–N_4-doped graphene for electroreduction of nitrate, ACS Catal. 12 (2022) 5407–5415.

[50] Y. Wang, D. Wu, P. Lv, B. He, X. Li, D. Ma, Y. Jia, Theoretical insights into the electroreduction of nitrate to ammonia on graphene-based single atom catalysts, Nanoscale 14 (2022) 10862.

[51] P.E. Blochl, Pojector augmented-wave method, Phys. Rev. B. 50 (1994) 17953–17979.

[52] G. Kresse, D. Joubert, From ultrasoft pseudopotentials to the projector augmented-wave method, Phys. Rev. B. 59 (1999) 1758–1775.

[53] J.P. Perdew, K. Burke, M. Ernzerhof, Generalized gradient approximation made simple, Phys. Rev. Lett. 77 (1996) 3865–3868.

[54] G. Kresse, J. Hafner, Ab initio molecular-dynamics for liquid-metals, Phys. Rev. B. 47 (1993) 558–561.

[55] G. Kresse, J. Furthmüller, Efficient iterative schemes for ab initio total-energy calculations using a plane-wave basis set, Phys. Rev. B. 54 (1996) 11169–11186.

[56] S. Grimme, Semiempirical GGA-type density functional constructed with a long-range dispersion correction, J. Comput. Chem. 27 (2006) 1787–1799.

[57] G. Henkelman, B.P. Uberuaga, H. Jónsson, A climbing image nudged elastic band method for finding saddle points and minimum energy paths, J. Chem. Phys. 113 (2000) 9901–9904.

[58] M. Yu, D.R. Trinkle, Accurate and efficient algorithm for Bader charge integration, J. Chem. Phys. 134 (2011), 064111.

[59] J.K. Nørskov, J. Rossmeisl, A. Logadottir, L. Lindqvist, J.R. Kitchin, T. Bligaard, H. Jonsson, Origin of the overpotential for oxygen reduction at a fuel-cell cathode, J. Phys. Chem. B. 108 (2004) 17886–17892.

[60] A.A. Peterson, F. Abild-Pedersen, F. Studt, J. Rossmeisl, J.K. Nørskov, How copper catalyzes the electroreduction of carbon dioxide into hydrocarbon fuels, Energy Environ. Sci. 3 (2010) 1311–1315.

[61] X. Zhou, J. Gao, Y. Hu, Z. Jin, K. Hu, K.M. Reddy, Q. Yuan, X. Lin, H.-J. Qiu, Theoretically revealed and experimentally demonstrated synergistic electronic interaction of CoFe dual-metal sites on N-doped carbon for boosting both oxygen reduction and evolution reactions, Nano Lett. 22 (2022) 3392–3399.

[62] L. Zhang, J.M.T.A. Fischer, Y. Jia, X. Yan, W. Xu, X. Wang, J. Chen, D. Yang, H. Liu, L. Zhuang, M. Hankel, D.J. Searles, K. Huang, S. Feng, C.L. Brown, X. Yao, Coordination of atomic Co–Pt coupling species at carbon defects as active sites for oxygen reduction reaction, J. Am. Chem. Soc. 140 (2018) 10757–10763.

[63] X. Zhao, R. Fang, F. Wang, X. Kong, Y. Li, Dual-metal single atoms with dual coordination for the domino synthesis of natural flavones, JACS Au 3 (2023) 185–194.

[64] T. Cui, Y.-P. Wang, T. Ye, J. Wu, Z. Chen, J. Li, Y. Lei, D. Wang, Y. Li, Engineering dual single-atom sites on 2D ultrathin N-doped carbon nanosheets attaining ultra-Low-temperature Zinc-air battery, Angew. Chem. Int. Ed. 61 (2022), e202115219.

[65] W. Zhang, Y. Chao, W. Zhang, J. Zhou, F. Lv, K. Wang, F. Lin, H. Luo, J. Li, M. Tong, E. Wang, S. Guo, Emerging dual-atomic-site catalysts for efficient energy catalysis, Adv. Mater. 33 (2021) 2102576.

[66] X. Zhao, F. Wang, X.-P. Kong, R. Fang, Y. Li, Dual-metal hetero-single-atoms with different coordination for efficient synergistic catalysis, J. Am. Chem. Soc. 143 (2021) 16068–16077.

[67] G. Wang, Y. Zhang, K. Chen, Y. Guo, K. Chu, PdP_2 nanoparticles on reduced graphene oxide: a catalyst for the electrocatalytic reduction of nitrate to ammonia, Inorg. Chem. 62 (2023) 6570–6575.

[68] G. Zhang, Y. Wan, H. Zhao, Y.-L. Guo, K. Chu, A metal-free catalyst for electrocatalytic NO reduction to NH_3, Dalton Trans. 52 (2023) 6248–6253.

[69] X.-F. Cheng, J.-H. He, H.-Q. Ji, H.-Y. Zhang, Q. Cao, W.-J. Sun, C.-L. Yan, J.-M. Lu, Coordination symmetry breaking of single-atom catalysts for robust and efficient nitrate electroreduction to ammonia, Adv. Mater. 34 (2022) 2205767.

[70] X. Zhang, C. Wang, Y. Guo, B. Zhang, Y. Wang, Y. Yu, Cu clusters/TiO_{2-x} with abundant oxygen vacancies for enhanced electrocatalytic nitrate reduction to ammonia, J. Mater. Chem. A. 10 (2022) 6448–6453.

[71] J. Wu, Y.-X. Yu, Highly selective electroreduction of nitrate to ammonia on a Ru-doped tetragonal Co_2P monolayer with low-limiting overpotential, Catal. Sci. Technol. 11 (2021) 7160–7170.

[72] J. Cai, Y. Wei, A. Cao, J. Huang, Z. Jiang, S. Lu, S.-Q. Zang, Electrocatalytic nitrate-to-ammonia conversion with ~100% Faradaic efficiency via single-atom alloying, Appl. Catal. B Environ. 316 (2022), 121683.

[73] Z.-L. Xie, D. Wang, X.-Q. Gong, Theoretical insights into nitrate reduction to ammonia over Pt/TiO_2: reaction mechanism, activity regulation, and catalyst design, ACS Catal. 12 (2022) 9887–9896.

[74] T. Hu, C. Wang, M. Wang, C.M. Li, C. Guo, Theoretical insights into superior nitrate reduction to ammonia performance of copper catalysts, ACS Catal. 11 (2021) 14417–14427.

[75] J.B. Geri, J.P. Shanahan, N.K. Szymczak, Testing the push–pull hypothesis: Lewis acid augmented N_2 activation at iron, J. Am. Chem. Soc. 139 (2017) 5952–5956.

[76] Y. Zang, Q. Wu, S. Wang, B. Huang, Y. Dai, Y. Ma, Activating dual atomic electrocatalysts for the nitric oxide reduction reaction through the P/S element, Mater. Horiz. 10 (2023) 2160–2168.

[77] K. Mathew, R. Sundararaman, K. Letchworth-Weaver, T. Arias, R.G. Hennig, Implicit solvation model for density-functional study of nanocrystal surfaces and reaction pathways, J. Chem. Phys. 140 (2014), 084106.

[78] Y. Liu, B. Song, C.-X. Huang, L.-M. Yang, Dual transition metal atoms embedded in N-doped graphene for electrochemical nitrogen fixation under ambient conditions, J. Mater. Chem. A. 10 (2022) 13527–13543.

[79] T. Deng, C. Cen, H. Shen, S. Wang, J. Guo, S. Cai, M. Deng, Atom-pair catalysts supported by N-doped graphene for the nitrogen reduction reaction: d-band center-based descriptor, J. Phys. Chem. Lett. 11 (2020) 6320–6329.

[80] X. Xie, L. Shang, X. Xiong, R. Shi, T. Zhang, Fe single-atom catalysts on MOF-5 derived carbon for efficient oxygen reduction reaction in proton exchange membrane fuel cells, Adv. Energy Mater. 12 (2022) 2102688.

[81] C. Gao, J. Low, R. Long, T. Kong, J. Zhu, Y. Xiong, Heterogeneous single-atom photocatalysts: fundamentals and applications, Chem. Rev. 120 (2020) 12175–12216.

[82] X. Li, P. Shen, Y. Luo, Y. Li, Y. Guo, H. Zhang, K. Chu, PdFe single-atom alloy metallene for N_2 electroreduction, Angew. Chem. Int. Ed. 134 (2022) e202205923.

[83] S.K. Kaiser, Z. Chen, D. Faust Akl, S. Mitchell, J. Pérez-Ramírez, Single-atom catalysts across the periodic table, Chem. Rev. 120 (2020) 11703–11809.

[84] H. Xu, Y. Zhao, Q. Wang, G. He, H. Chen, Supports promote single-atom catalysts toward advanced electrocatalysis, Coord. Chem. Rev. 451 (2022), 214261.

[85] K. Chen, Z. Ma, X. Li, J. Kang, D. Ma, K. Chu, Single-atom Bi alloyed Pd metallene for nitrate electroreduction to ammonia, Adv. Funct. Mater. 33 (2023) 2209890.